Supporting Information

Dixon et al. 10.1073/pnas.1412299111

GPS Data Analysis

GPS data analysis and error estimation follow ref. 1. Briefly, GPS observations are used to estimate 24-h average positions, using the GIPSY/OASIS (GPS Inferred Positioning System/Orbit Analysis Software) software in the precise point positioning mode (2). Observations with less than 4 h of observations are deleted. Fiducial-free orbit data from the Jet Propulsion Lab are used to produce fiducial-free station coordinates. Daily site coordinates are then transformed to the ITRF (International Terrestrial Reference Frame) 2008 reference frame (3) using daily transformation parameters also provided by the Jet Propulsion Lab. The Wide Lane Phase Bias (4) solutions are adopted for calculating cycle ambiguities in the GPS observations. This algorithm is able to resolve ambiguities with single station observations, which improves the GPS time series repeatability by ~30% in the east direction. The postfit WRMS (weighted root mean square scatter) for a linear plus seasonal time series model fit to the raw position data are 3 mm, 3 mm, and 8 mm for the north, east, and vertical components, respectively. Regional filtering (5) and modeling the SSEs (1) reduces postfit WRMS to 2 mm, 2 mm, and 6 mm for the three position components. The positionogram method (1) is used to identify the onset of the SSEs in the GPS time series. Velocity uncertainties from analysis of the GPS postfit residuals using a white plus colored noise model are 0.1 mm/y for the horizontal component estimates and 0.5 mm/y for the vertical component.

All velocities from the GPS time series are initially in the ITRF 2008 reference frame. A local rotation pole is used to transform these to the stable Caribbean Plate reference frame (6) following procedures outlined in our previous studies (1, 7–9). A model for the GPS time series is then developed that accounts for inter-SSE velocity, seasonal variation, and SSE timing, duration, and displacement (1).

Inversions for Slip at Depth

We use the TDefnode software package (10) to invert our geodetic measurements. TDefnode simultaneously estimates long-term block rotation, interseismic or inter-SSE locking on fault surfaces, and transient sources such as SSEs. The Earth's crust is defined by a series of plates or blocks separated by active faults. Block motions are specified by rotation about Euler poles, and strain accumulation along block boundaries is specified by the backslip model (11). Block boundaries are faults that are represented by 3D irregular grids of nodes defined by latitude, longitude, and depth. For this work, the fore-arc block (8, 9) is defined separately from the Cocos and Caribbean plates. The fore-arc block is bounded by a right-lateral strike-slip fault to the northeast and the dipping subduction interface to the southwest. The strike slip fault separating the fore-arc block and Caribbean plate is assumed to be vertical and to run through the active volcanic chain. The thrust fault separating the fore-arc block from the Cocos plate dips at a value specified by the slab model (12). Additional constraints include Centroid Moment Tensor earthquake slip vectors and campaign GPS stations to help define the relative motion direction between the fore-arc block and adjacent plates.

Strain accumulation in adjacent blocks due to locking on block boundaries is calculated by adopting elastic Green's functions and integrating over small patches between the nodes. Surface velocities are predicted using Okada's method (13), applying a slip deficit rate on each small patch defined by adjacent nodes. To quantify inter-SSE locking along the plate interface, a locking factor *phi* is estimated for each node, defined as the ratio of locked to total slip on the fault, ranging from 0 (freely slipping) to 1 (fully locked), and then smoothed. The inversion scheme uses a grid search and simulated annealing (14) to seek the set of parameters that minimizes data misfit, defined by the reduced χ^2 statistic. To reduce the number of estimated parameters when inverting for the inter-SSE locking pattern, rake is determined by the relative plate or block motion direction.

For SSEs, two approaches were compared: Slip direction is opposite to the direction of plate motion, and slip direction is estimated as a free parameter. In both cases, slip direction (rake) is assumed uniform over the entire plate interface in both space and time; that is, rake variation between patches is not allowed. Results for the two approaches are similar; here we present the case where rake is estimated.

Different along-strike and down-dip parameterization methods for inter-SSE locking and slow slip can also be used to reduce the number of adjustable parameters. In this study, we use the free nodes ("smoothed grid" method) (10) for both inter-SSE locking and SSE displacement to obtain unbiased estimates of patch shape, smoothing results to better represent the inherent spatial resolution of the network, ~30 km (*Spatial Resolution of the Inversions*). We tested the stability of results by performing a large number of inversions under various data weighting and smoothing conditions. Note that results for the 2007.4 SSE are very similar to those presented in ref. 7 even though the data analysis and inversion procedures differ substantially between the two studies. This event is more poorly constrained than later events (*Spatial Resolution of the Inversions*).

Spatial Resolution of the Inversions

Although the node spacing (~10 km beneath the peninsula, somewhat larger offshore) of our mesh can yield slip patch estimates with the same dimensions, this exceeds the inherent spatial resolution of our network, which has a typical station spacing of ~20–30 km. Some form of regularization of the inversion is therefore required. Inversion results (for both inter-SSE locking and SSEs) are therefore smoothed to better reflect network resolution. An initial series of inversions is run to define the tradeoff between smoothing and data misfit; smoothed solutions with data misfit comparable to the known data noise (1) are deemed acceptable (Fig. S1).

We checked the spatial resolving power of the network for inter-SSE locking by conducting a series of "checkerboard" tests, similar to that described in ref. 9. Adjacent patches are assigned to be either fully locked or fully slipping, the corresponding surface displacement is calculated at the existing station locations, random noise is added, and the synthetic dataset is inverted, in this case without smoothing to better illustrate whether individual patches are well-resolved. The test is repeated for various patch sizes, starting with a small patch size (~10 km) and then in multiples of this patch size (~20 km, 30 km, and 40 km). It can be seen in Fig. S2 that patch sizes of 10 and 20 km (*Top*) are not well-resolved. The 30-km patch sizes (third panel) are well-resolved beneath the peninsula, but are less well-resolved offshore. The 40-km patches (*Bottom*) are resolved offshore out to a distance of ~30 km and are less well-resolved beyond this distance.

The resolution of SSE slip patches is similar to the inter-SSE locking, unless individual stations are offline during an event. Fig. S3 shows where the spatial resolution of SSEs is strong (90% or more of the simulated slip is recovered) and moderate (60% or more recovery) assuming a fully operational network. Of course, this is not always the case. As an example, coastal station SAJU only came online in 2008; hence, the 2007.4 SSE is less well-constrained compared with later events. Nevertheless, our solution for the 2007.4 SSE appears to be robust; different data weighting and inversion schemes yield similar results.

A Possible Earthquake Precursor and Coulomb Failure Stress Analysis

An SSE started several months before the 2012 earthquake and continued right up until the time of the earthquake (Fig. 1 and Fig. S4). To assess the possibility that slow slip triggered the 2012 earthquake, we calculated the stress change associated with slow slip at the point where the earthquake nucleated, and other locations on the plate interface. Coulomb Failure Stress changes (ΔCFS) were calculated using Coulomb 3.3 software (15). ΔCFS is a relationship between shear stress change and normal stress change:

$$\Delta CFS = \Delta\tau - \mu'\Delta\sigma_n,$$

where $\Delta\tau$ is the change in shear stress, μ' is the effective friction, and $\Delta\sigma_n$ is the change in normal stress (15, 16). A positive value for ΔCFS implies that the fault is brought closer to failure. We use the slip distribution from the inversion averaged over a subfault grid, which is 18 × 16 patches. The geometry of the patches is consistent with the Slab 1.0 model (12). In these calculations, we assume a rake of 128° (17) and $\mu' = 0.4$. If we consider the hypocenter for the 2012 earthquake (17), 9.75° N and 274.5° E, with a depth of 16 km (green star in Fig. S5), the ΔCFS from the 2012 SSE is +0.128 bars.

ΔCFS is inherently dependent on fault orientation. Experimentation with the "receiver" fault orientation gives ΔCFS as high as +0.2 bars and as low as –0.15 bars. These extreme values were calculated for a fault dipping at 10° at the hypocenter (17) with rakes of 160° and 0°, respectively. The dip of 10° coincides with the dip of the Slab 1.0 fault model (12), however the range of rakes extends beyond realistic values for subduction zone thrust faulting. Varying the receiver fault dip from 5–30° does not change ΔCFS significantly (<0.05 bars). Using other reported hypocenters from the US Geological Survey, National Earthquake Information Center, located closer to the center of the peninsula, gives a ΔCFS lower than that of our preferred hypocenter (17). Although sections of the fault located near the SSE patches experienced ΔCFS as high as +0.5 bars, these patches are not located near the preferred hypocenter for the 2012 $M_w = 7.6$ event.

Hence, although the timing of the 2012 SSE is suspiciously close to the 2012 earthquake, and the direction of motion of several GPS stations is somewhat anomalous compared with previous SSEs, a clear case for triggering of the 2012 earthquake by a SSE cannot be made. Given existing data and models, we cannot preclude the possibility that the timing of the 2012 SSE and the 2012 earthquake was coincidental.

Plate Interface Geometry

To define the geometry of the plate interface for both the SSEs and the ΔCFS analysis, we use the Slab 1.0 model (12). This published, open source, 3D global model is now widely used for subduction zone strain and related calculations but can differ from models augmented by local seismic data. We compared the Slab 1.0 model to several other published local models, including a recent 2D model (18) and another 3D model (19) (Fig. S6). All of these models are very similar in the depth range of 0–20 km (the depth range of shallow SSEs), typically within a 3 km depth or better at a given distance from the trench. However, below 20 depth (e.g., including the region of deeper SSEs), the models can differ by 10–15 km in predicted depth at a given distance from the trench. In the northern Nicoya Peninsula, Slab 1.0 and the model of Christeson et al. (20) are very similar, whereas the other models are about 10 km deeper at a distance of 100 km from the trench. In the southern Nicoya Peninsula, Slab 1.0 and the models of DeShon et al. (19) and Christeson et al. (20) are very similar, whereas the other models are about 10–15 km deeper at this distance from the trench.

These differences do not significantly affect estimates of the location of the deeper SSEs shown in Figs. 3 and 4, which show the projection of these events onto the horizontal surface. Hence, the assignment of deeper SSEs to the region of the plate interface below the seismic rupture patch is unaffected by choice of plate interface model. The ΔCFS estimates are similarly little affected by the choice of plate boundary geometry. However, choice of plate interface model does affect the interpretation of depth, which is important when assessing physical conditions on the plate interface, such as pressure and temperature.

1. Jiang Y, et al. (2012) Slow slip events in Costa Rica detected by continuous GPS observations, 2002-2011. *Geochem Geophys Geosyst* 13:Q04006.
2. Zumberge JF, Heflin MB, Jefferson DC, Watkins MM, Webb FH (1997) Precise point positioning for the efficient and robust analysis of GPS data from large networks. *J Geophys Res* 102:5005–5017.
3. Altamimi Z, et al. (2011) ITRF2008: An improved solution of the international terrestrial reference frame. *J Geod* 85:457–473.
4. Bertiger WS, et al. (2010) Single receiver phase ambiguity resolution with GPS data. *J Geod* 84:327–337.
5. Wdowinski S, et al. (1997) Southern California Permanent GPS Geodetic Array: Spatial filtering of daily positions for estimating coseismic and postseismic displacements induced by the 1992 Landers earthquake. *J Geophys Res* 102:18,057–18,070.
6. DeMets C (2001) A new estimate for present day Cocos & Caribbean Plate motion: Implications for slip along the Central American Volcanic Arc. *Geophys Res Lett* 28: 4043–4046.
7. Outerbridge KC, et al. (2010) A tremor and slip event on the Cocos-Caribbean subduction zone as measured by a global positioning system (GPS) and seismic network on the Nicoya Peninsula, Costa Rica. *J Geophys Res* 115:B10408.
8. LaFemina P, et al. (2009) Fore-arc motion and Cocos Ridge collision in Central America. *Geochem Geophys Geosys* 10:Q05S14.
9. Norabuena E, et al. (2004) Geodetic and seismic constraints on some seismogenic zone processes in Costa Rica. *J Geophys Res* 109:B11403.
10. McCaffrey R (2009) Time dependent inversion of three component continuous GPS for steady and transient sources in northern Cascadia. *Geophys Res Lett* 36:L07304.
11. Savage JC (1983) A dislocation model of strain accumulation and release at a subduction zone. *J Geophys Res* 88:4984–4996.
12. Hayes GP, Wald DJ, Johnson RL (2012) Slab1.0: A three-dimensional model of global subduction zone geometries. *J Geophys Res* 117:B01302.
13. Okada Y (1985) Surface deformation due to shear and tensile faults in a half-space. *Bull Seismol Soc Am* 75:1135–1154.
14. Press WH, Teukolsky SA, Vetterling WT, Flannery BP (2007) *Numerical Recipes: The Art of Scientific Computing* (Cambridge Univ Press, New York), 3rd Ed.
15. Toda S, Stein RS, Sevilgen V, Lin J (2011) *Coulomb 3.3 Graphic-Rich Deformation and Stress-Change Software for Earthquake, Tectonic, and Volcano Research and Teaching—User Guide* (U.S. Geological Survey Open-File Report), Vol 2011–1060, 63 pp.
16. Stein RS, Barka AA, Dieterich JH (1997) Progressive failure on the North Anatolian fault since 1939 by earthquake stress triggering. *Geophys J Int* 128:594–604.
17. Yue H, et al. (2013) The 5 September 2012 Costa Rica M_w 7.6 earthquake rupture process from joint inversion of high-rate GPS, strong-motion, and teleseismic P wave data and its relationship to adjacent plate boundary interface properties. *J Geophys Res* 118:5453–5466.
18. Feng L, et al. (2012) Active deformation near the Nicoya Peninsula, northwestern Costa Rica, between 1996 and 2010: Interseismic megathrust coupling. *J Geophys Res* 117, 10.1029/2012JB009230.
19. DeShon HR, et al. (2006) Seismogenic zone structure beneath the Nicoya Peninsula, Costa Rica, from three-dimensional local earthquake P- and S-wave tomography. *Geophys J Int* 164:109–124.
20. Christeson GL, McIntosh KD, Shipley TH, Flueh ER, Goedde H (1999) Structure of the Costa Rica convergent margin, offshore Nicoya Peninsula. *J Geophys Res* 104: 25,443–25,468.

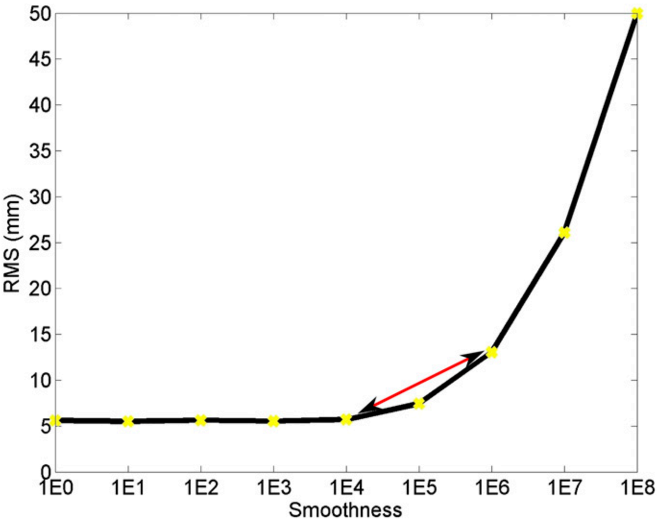

Fig. S1. Tradeoff between smoothing of inversion results for SSEs and rms misfit of model to data. Smoothing values between 10^4 and 10^6 were investigated in this study (arrows).

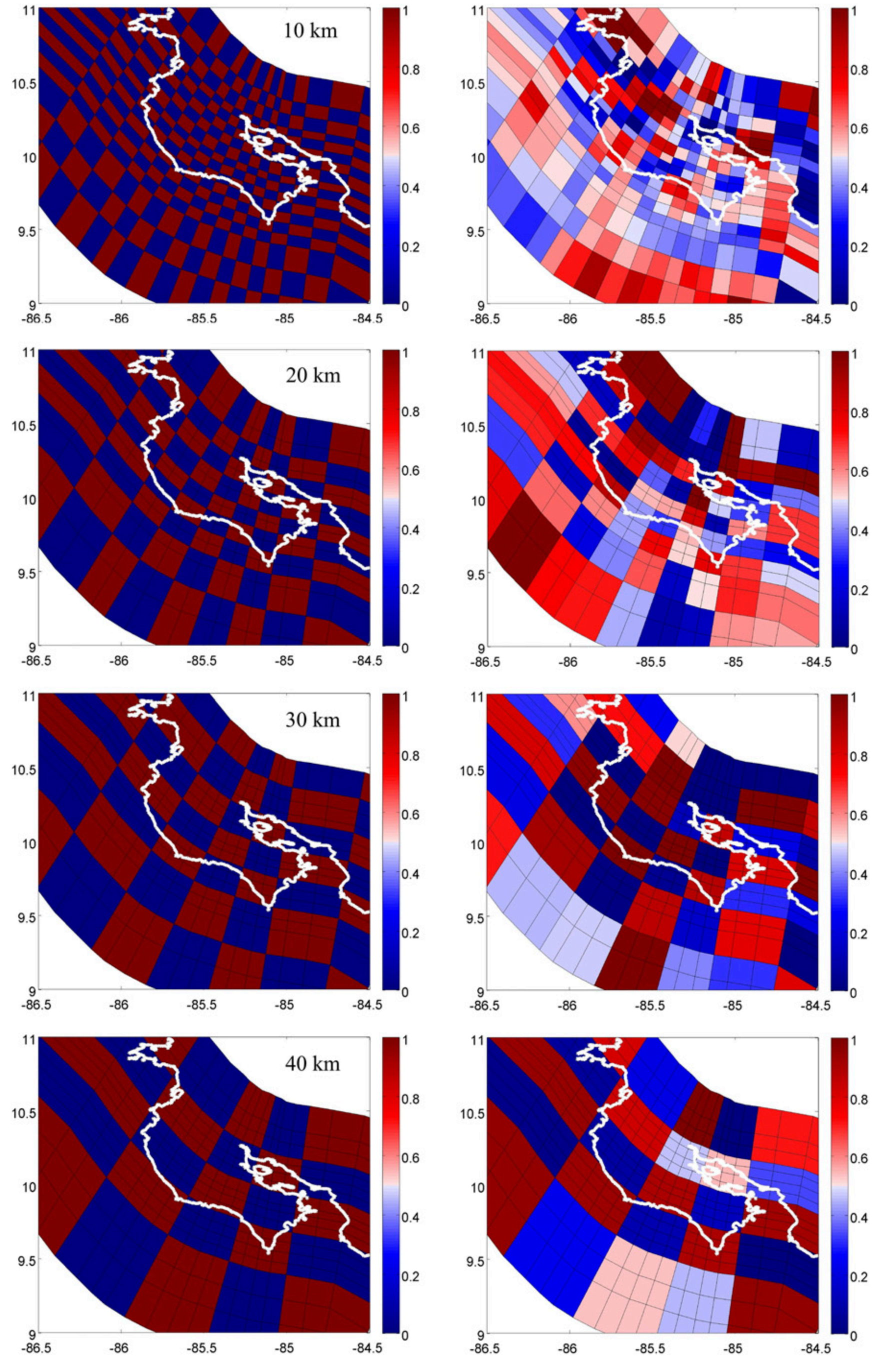

Fig. S2. Checkerboard test of network and inversion resolution. Four different patch sizes are used to determine the minimum resolvable patch size for inter-SSE locking or slow slip (*Left*, input; *Right*, output). The 30-km patches (third panel from top) are resolvable beneath the peninsula. Immediately offshore, 30-km patches are resolvable in some areas, degrading to ~40 km farther offshore (*Bottom*).

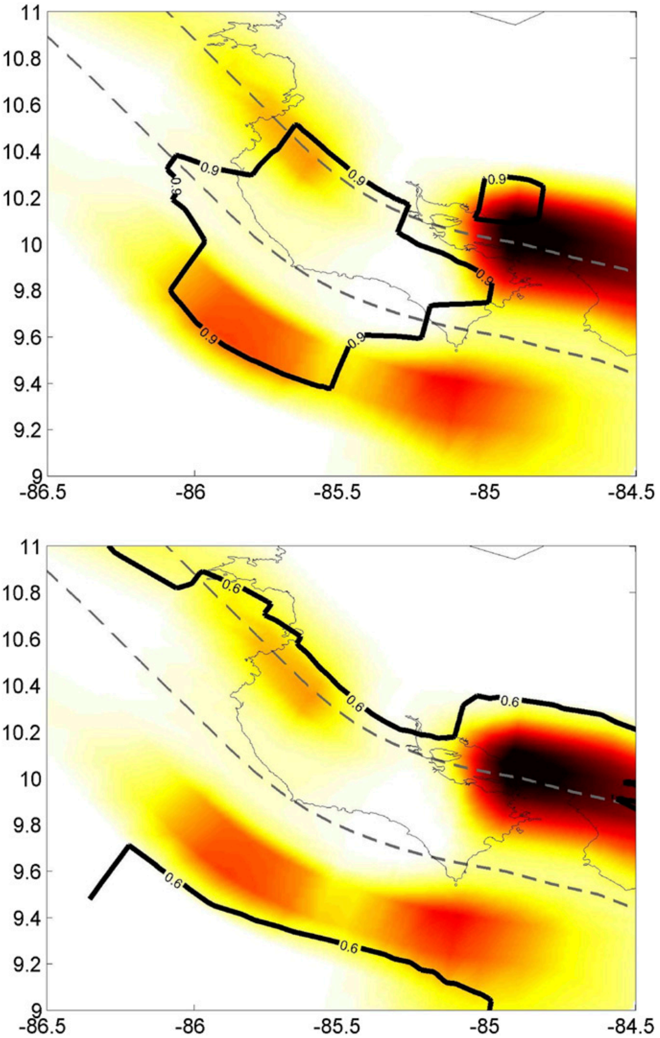

Fig. S3. Summed slip for all SSEs from 2007 to 2012, compared with resolution of slip estimates. (*Top*) Contours outline area where resolution is strong (>90% of simulated slip is recovered by inversion). (*Bottom*) Contours outline areas where resolution is weaker (>60% of simulated slip is recovered by inversion).

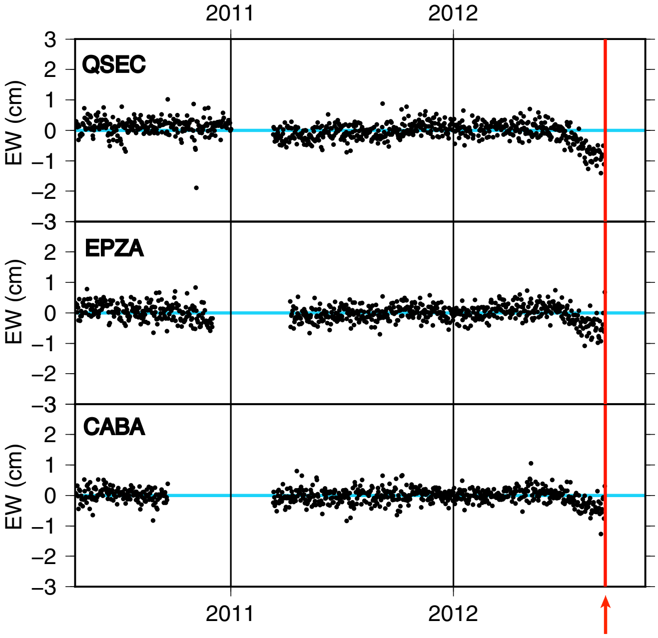

Fig. S4. Detrended displacement time series for the east–west component of three high-precision GPS stations in the Nicoya Peninsula, Costa Rica for 2 y before the 5 September 2012 earthquake (red line and arrow). An SSE beginning several months before the earthquake is evident in all three stations, continuing up to the day of the earthquake.

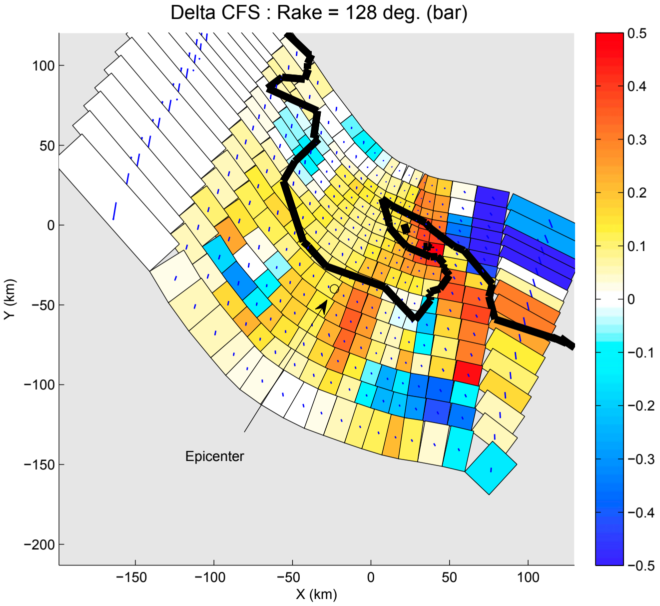

Fig. S5. ΔCFS associated with the 2012 SSE. Red colors indicate changes promoting earthquake rupture, and blue colors indicate changes inhibiting earthquake rupture. Circle and arrow mark the location of rupture initiation of the 2012 earthquake (1).

1. Yue H, et al. (2013) The 5 September 2012 Costa Rica M_w 7.6 earthquake rupture process from joint inversion of high-rate GPS, strong-motion, and teleseismic P wave data and its relationship to adjacent plate boundary interface properties. *J Geophys Res* 118:5453–5466.

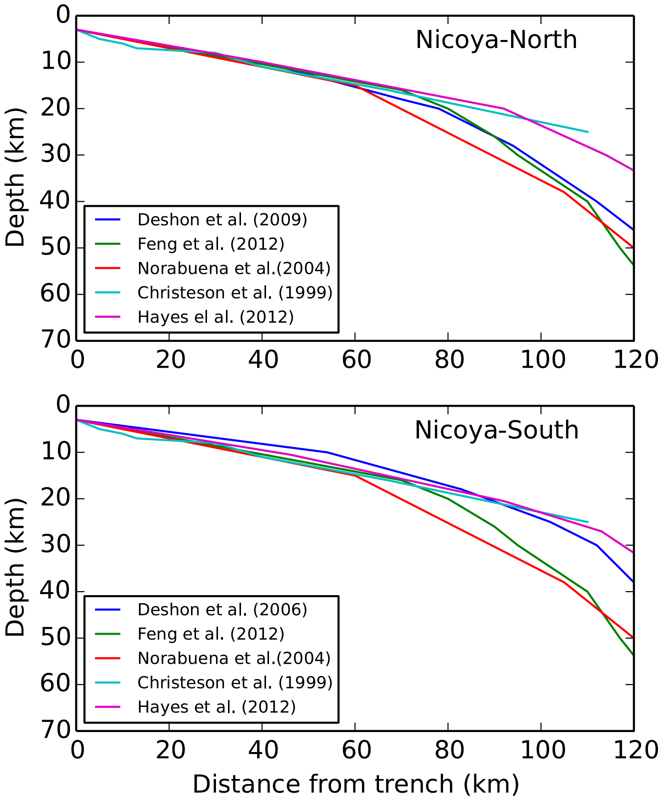

Fig. S6. Comparison of different models for slab geometries beneath the Nicoya Peninsula. Cross-sections are perpendicular to the local trend of the trench. Model references include the following: DeShon et al. (2006) (1), Feng et al. (2013) (2), Norabuena et al. (2004) (3), Christeson et al. (1999) (4), and Hayes et al. (2012) (5).

1. DeShon HR, et al. (2006) Seismogenic zone structure beneath the Nicoya Peninsula, Costa Rica, from three-dimensional local earthquake P- and S-wave tomography. *Geophys J Int* 164: 109–124.
2. Feng L, et al. (2012) Active deformation near the Nicoya Peninsula, northwestern Costa Rica, between 1996 and 2010: Interseismic megathrust coupling. *J Geophys Res* 117, 10.1029/2012JB009230.
3. Norabuena E, et al. (2004) Geodetic and seismic constraints on some seismogenic zone processes in Costa Rica. *J Geophys Res* 109:B11403.
4. Christeson GL, McIntosh KD, Shipley TH, Flueh ER, Goedde H (1999) Structure of the Costa Rica convergent margin, offshore Nicoya Peninsula. *J Geophys Res* 104:25,443–25,468.
5. Hayes GP, Wald DJ, Johnson RL (2012) Slab1.0: A three-dimensional model of global subduction zone geometries. *J Geophys Res* 117:B01302.